2016

Unequal a priori Probability Multiple Hypothesis Testing in Space Domain Awareness with the Space Surveillance Telescope

Tyler J. Hardy

Stephen C. Cain
Air Force Institute of Technology

Travis F. Blake

Recommended Citation

Hardy, T. J., Cain, S. C., & Blake, T. F. (2016). Unequal a priori probability multiple hypothesis testing in space domain awareness with the space surveillance telescope. Applied Optics, 55(15), 4036–4046. https://doi.org/10.1364/AO.55.004036

Journal:	*Applied Optics*
Article Title:	Unequal a priori probability multiple hypothesis testing in space domain awareness with the space surveillance telescope
Authors:	Tyler Hardy, Stephen Cain, and Travis Blake
Accepted for publication:	21 April 2016
Final version published:	13 May 2016
DOI:	http://dx.doi.org/10.1364/AO.55.004036

Unequal A Priori Probability Multiple Hypothesis Testing in Space Domain Awareness with the Space Surveillance Telescope

Tyler Hardy,[1] Stephen Cain,[1] and Travis Blake[2]
[1]*Air Force Institute of Technology, 2950 Hobson Way, Dayton, OH 45433*
[2]*Lockheed Martin Space Systems Company, 13560 Dulles Technology Drive, Herndon, VA 20171*

This paper investigates the ability to improve Space Domain Awareness (SDA) by increasing the number of detectable Resident Space Objects (RSOs) from space surveillance sensors. With matched filter based techniques the expected impulse response, or Point Spread Function (PSF), is compared against the received data. In the situation where the images are spatially undersampled, the modeled PSF may not match the received data if the RSO does not fall in the center of the pixel. This aliasing can be accounted for with a Multiple Hypothesis Test (MHT). Previously, proposed MHTs have implemented a test with an equal a priori prior probability assumption. This paper investigates using an unequal a priori probability MHT. To determine accurate a priori probabilities three metrics are computed; they are correlation, physical distance, and empirical. Using the calculated a priori probabilities, a new algorithm is developed and images from the Space Surveillance Telescope (SST) are analyzed. The number of detected objects by both an equal- and unequal- prior probabilities are compared while keeping the false alarm rate constant. Any additional number of detected objects will help improve SDA capabilities.

OCIS codes: (040.0040) Detectors; (040.1880) Detection; (100.0100) Image Processing; (110.6770) Telescopes.

I. INTRODUCTION

The purpose of this research is to increase Space Domain Awareness (SDA) capabilities by proposing a new detection algorithm that improves the probability of detecting space objects. This is done by investigating a new set of a priori probabilities in a Bayes Risk based Multiple Hypothesis Test (MHT) proposed in [1].

SDA is the comprehensive understanding of everything associated with the space domain and involves several factors including the detection, tracking, and characterization of space objects. These objects can include satellites and orbital debris. An important objective of SDA is to be able to detect, track, and characterize these Resident Space Objects (RSOs). Depending on where the objects are located, the size of the objects, and how the objects need to be characterized, different methods of collection are used. These methods include both ground- and space-based optical systems, as well as ground-based radars.

There are multiple stakeholders in SDA data collection. They include the Department of Defense (DoD) and other U.S. and foreign government agencies. These agencies have published space policies that include improving SDA data collection as a cornerstone of their organization [2–4]. One of the core tenants of the policies is the responsible use of space and the prevention of collisions in space that could prevent the effective use of space capabilities due to a dense space debris environment. It is critical that space objects in orbit are catalogued to mitigate the potential to cause severe damage to space assets. Avoiding space objects is critical to maintaining functional space assets and retaining a tactical edge in the space domain.

This paper focuses on a ground-based SDA survey telescope system, the SST. The SST is a Mersenne-Schmidt telescope developed by MIT Lincoln Labs as a Defense Advanced Research Projects Agency (DARPA) program [5]. The stated mission of the SST program is "to enable ground-based, broad-area search, detection and tracking of small objects in deep space for purposes such as space mission assurance and asteroid detection" [6]. The SST is currently located at the White Sands Missile Range in New Mexico. The SST is a large field-of-view telescope with the ability to quickly scan the night sky and detect and track objects primarily located in Geosynchronous Earth Orbit (GEO), as well as deep space objects. Information collected by the SST is used for achieving the goals outlined in U.S. space policies and keeping a robust and accurate SDA picture. Any improvements in the ability of the SST to detect objects in orbit will help in meeting this goal of improved detection and characterization of space objects. Table I contains SST parameters relevant to this research.

TABLE I: Important SST system parameters used in this paper.

Parameter	**Value**
Focal length, f	3.5m
Primary mirror/obscuration	3.5m / 1.75m
Pixel size	15μm x 15μm
Total number pixels	6144x4096
Center wavelength, $\bar{\lambda}$	500nm

In addition to the detection of objects in orbit, detecting Near-Earth Asteroids (NEAs) is another part of

SST's mission. The National Aeronautics and Space Administration (NASA) has been tasked with detecting 90 percent of the NEAs that pose a severe threat to humankind by 2020 [7]. These objects are defined as asteroids larger than 140m in diameter that have a perihelion distance of less than 1.3 Astronomical Units from the sun. In a 2010 National Research Council (NRC) report on the progress towards this goal, it was determined that the survey would not be completed by 2020 [8]. One major deficiency identified was the lack of necessary funding. These conclusions were further detailed in a 2014 NASA Inspector General report [9]. At the time of this report, NASA believes they currently have surveyed 10 percent of the 90 percent goal, with many of those surveyed objects being larger than 1km. Due to lack of necessary funding, as stated in these reports, there is a significant benefit to utilizing existing telescope systems to improve SDA data collection efforts. Improving the ability of the SST to detect dimmer and smaller objects will improve the progression towards the mandated goal, with little or no additional cost or hardware.

Improving the ability to detect RSOs and NEAs can be accomplished in many ways. Increasing the size of the telescope optics, improved Charge-Coupled Device (CCD) technology, and higher quality optical elements are three examples of hardware improvements that increase performance. These upgrades come at a significant cost to the program and have practical limitations due to shipping logistics and other constraints. On the other hand, a new method of processing the data resulting in more detections accomplishes the same objective with little to no additional cost to the program. There have been several approaches investigated to improve the detection performance of SDA telescopes using only data processing improvements. These approaches are discussed in section II A.

Section II covers relevant background research and topics, section III describes important theory on the optical model and the detection algorithm, and section IV discusses the experiment used to determine the effectiveness of this algorithm. Section V covers the results and section VI frames the results and presents the conclusions from this research.

II. BACKGROUND

In this section an overview of previous SDA detection algorithms are discussed, as well as the motivation for the new MHT presented in this paper. There are three important factors that impact the types of algorithms that are developed, and their effectiveness in detecting RSOs.

- Decisions about an object are made only by the data available in a single frame or captured image. The persistence of RSOs may be noted frame to frame to reduce false alarms, as is done in with the SST.

- The frames are collected with long exposure imaging, greater than 10ms [10], but not long enough to cause objects moving at sidereal rate to streak.

- All observed objects are unresolved point sources to the system. The apparent size of space objects on the detector are not necessarily limited to one pixel due to optical aberrations or atmospheric effects.

A. SDA Detection Algorithms

The SST program is not the first or only program to collect SDA information. Before the use of CCD technology, searches for space objects were conducted by two primary methods. The first method used only the human eye and memory or note-taking. Observers could determine differences in object position over time to locate asteroids. When photograph technology was developed, comparing film images allowed for detailed studies of changes over time. Film comparison is more exact, but still requires manual analysis. This type of analysis limits the quantity of information that can be processed and the complexity of algorithms that can be used.

A large advancement occurred with the Spacewatch program and the advent of digital detection techniques in the 1980s [11]. With this new technology, moving objects could be automatically isolated by using algorithms. As the importance of space and SDA rose additional programs and research efforts were developed to advance knowledge about space objects. One of these programs is the Lincoln Near Earth Asteroid Research (LINEAR) program. LINEAR uses a Ground-based Electro-Optical Deep Space Surveillance (GEODSS) telescope to detect asteroids and utilizes a Binary Hypothesis Test (BHT) point detector to generate a binary map of ones and zeros signifying where objects are present [12]. In a BHT point detector, decisions are made by only investigating a single pixel and deciding between an object being present or not present.

With the increase in computer memory and processing speed, more advanced detection algorithms have become possible. Methods that do more than compare single pixels against a threshold provide greater detection ability at the cost of processing complexity. Using the expected image of an object viewed as a point source, or Point Spread Function (PSF), to search and make detection decisions is known as a matched filter. This method allows more than a single pixel to be used in the detection decision. Matched filtering effectively averages the noise over all the pixels used. One current standard for a matched filter algorithm used in multiple NEA programs is SExtractor, described in [13]. This is a software package that processes astronomical images and performs detection and classification. The portion that relates to this paper is the detection, or thresholding, step. The authors propose a method of convolution between the received data and the PSF for faint unresolved objects, the type of objects investigated in this paper. Additional methods applying SExtractor and improving the algorithm can be found in [14, 15]. These improvements still utilize the traditional matched filter technique.

Matched filter space object detectors can be separated into two categories: spatial only, and spatial and temporal. In a spatial only target detection, only the spatial characteristics of the object being investigated are utilized in the detection process, which can include the shape and intensity distribution. This type of algorithm is used when the object does not move significantly during the integration time of the image. Matched filter algorithms in space and time are also utilized for detection of space objects. In these algorithms, the spatial and temporal characteristics are both used to make detection decisions [16, 17]. These detection algorithms are not investigated further in this paper because they do not match the data collection methods used in the SST, where the integration time does not allow for significant orbital motion during collection. In spatial matched filtering, it is important to have an accurate model or prediction of what the object is expected to look like in the imaging system. In [18], the author showed that spatial sampling of the CCD pixels impacts the resulting image. The author investigates the effects of sampling at both Rayleigh and Nyquist rates, and demonstrates the impact on detection performance of a matched filter in undersampled systems.

Previous research in this area also addressed different models for the received noise distribution. The intensity data captured by the telescope also contains several sources of noise. There are dark current and other noise sources present in the CCD [19], photon counting noise [10], as well as background light from street lights and other ground-based noise sources. To implement these detection algorithms, it is essential to apply a model for the received noise. There have been several approaches used from Poisson [17, 20], to Gaussian [1, 21], to composite model that attempt to combine multiple effects [22]. The noise in this paper is assumed to be Gaussian, more details are discussed in section III A.

The methods described thus far all rely on deciding between two hypotheses. This is known as a BHT. Another approach that expands upon the idea of the BHT matched filter is a MHT. In contrast to the BHT matched filter and point detector, the MHT presents multiple PSF models to compare against the data. In this research area, a MHT is useful in situations where spatial undersampling occurs. In [1, 21], methods for increasing the detection performance in undersampled systems is presented. More details on the spatial undersampling and motivations for a MHT are discussed in section II B.

B. MHT Motivation and Background

The primary motivation for using a MHT is to overcome the effects of undersampling by the CCD pixels. If a telescope system is spatially undersampled, a small shift of where an object is formed within a single pixel can result in a different shape or distribution of intensity. Instead of shifting and retaining the spatial information, an aliased PSF loses spatial information and can have a different shape completely. This presents a problem in matched filter-based detection algorithms, where the goal is to find similar PSFs in the data. Figure 1 shows an example of a undersampled PSF model generated with a small sub-pixel shift

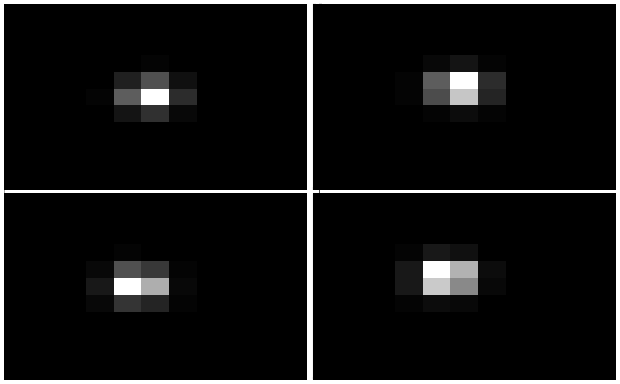

FIG. 1: Example of four PSFs impacted by undersampling spatially. The PSF have shifted, but also changed in shape and intensity.

A common method of determining the sampling required is using angular resolution found through a Rayleigh criterion. In [18] it is shown that in a matched filter detection algorithm Nyquist sampling performs better than Rayleigh. The required Nyquist sampling is found by combining the maximum frequency present in a diffraction limited system with the Nyquist theorem on required sampling. This gives the following required spatial sampling, Δ_s [23]:

$$\Delta_s = \frac{\bar{\lambda} f}{2d} \tag{1}$$

where $\bar{\lambda}$ is the center wavelength observed, f is focal length of the system, and d is the diameter of the pupil. Substituting the SST parameters into equation (1), a center wavelength of 500nm with a focal length and pupil diameter of 3.5m, gives a required sampling size of 0.25μm. The SST pixels are 15μm square, but are grouped 2x2 in these data collections. The binned pixels give an actual sampling size of 30μm. The difference between required and actual sampling in this case is 120 times. If the system is not diffraction limited, the actual undersampling factor will be much less. This is due to the pupil diameter d being limited by the effective seeing parameter, r_o. Seeing parameter values change depending on atmospheric conditions but are typically smaller than 10cm.

To make a decision if an object is present, a Bayes Criterion is used [24]. This equation provides a method of choosing the hypothesis that results in less risk $\mathcal{R}$ on average.

$$\mathcal{R} = \sum_{i=0}^{M-1} \sum_{k=0}^{M-1} \pi_k C_{ik} \int_{Z_i} p(\mathbf{D}|H_k) d\mathbf{D} \tag{2}$$

M is the total number of hypotheses considered. The cost, C_{ik}, represents the impact of choosing hypothesis i when hypothesis k has occurred. The value of C_{ik} ranges from zero to one, with one giving the largest cost penalty to a decision. The prior probabilities, π_k, represent how likely each potential hypothesis is to occur. The priors range between zero and one, and must sum to a total of one. When using a Bayes Criterion-based MHT there are several variables that impact the algorithm that results from the hypothesis test. The two discussed in this paper are the costs, C_{ik} and the a priori probabilities, π_k. $\mathbf{D}$ is a matrix containing one single frame of data. H_k is the k^{th} hypothesis. H_0 is the null hypothesis, where it is assumed that no space object is present. H_1 through H_{M-1} are the alternate hypotheses. These correspond to instances where the space object is considered present, and each hypothesis signifies a different sub-pixel position. These sub-pixel positions are described in section III C.

Different cost and a priori probability approaches have been researched, and each has potential benefits and drawbacks. The first area of difference is the assignment of cost. An equal-cost test, originally proposed in [21], penalizes the algorithm for incorrectly deciding between two alternate hypotheses. This emphasis on determining the correct sub-pixel position can lead to more accurate sub-pixel position estimates, potentially at the cost of the detection of space objects. Alternatively, an unequal-cost assumption will not penalize for selecting the wrong alternate hypothesis as long as an object is correctly detected [1]. Unequal-cost algorithms are more computationally complex and do not reduce to a Signal to Noise Ratio (SNR) sufficient statistic. Unequal-cost algorithms are not investigated in this paper.

The other area where a different assumption can be made is in a Bayes Risk MHT is the a priori probabilities. In this paper two different a priori probability approaches are investigated. They are an Equal-Cost Equal-Prior (ECEP) and an Equal-Cost Unequal-Prior (ECUP). ECEP assumes the following cost and probability assignment:

$$C_{ik} = \begin{cases} 0, & i = k \\ 1, & i \neq k \end{cases}, \qquad \pi_k = \frac{1}{M}. \tag{3}$$

For ECUP the same cost assumption applies. However the prior probability, π_k, for each hypothesis k is not $\frac{1}{M}$ and not necessarily the same. The prior probabilities are typically assumed to be equal if there is no prior knowledge of the system or method of determining accurate values for π_k. This paper considers several methods for finding accurate prior probability values and determines if more space objects can be found with the resulting algorithm.

Unequal prior probability has use in other research areas outside of SDA and space object detection. Often in cases where the input conditions might change, and adapting the assumptions or inputs to the algorithm may provide additional performance. These input conditions are the prior probabilities. Cognitive radar [25], neural networks [26] and adaptive algorithms [27, 28], Bayes estimators [29], and quantization of prior probabilities [30] are research areas that have investigated this effect. In some cases the focus is comparing equal vs. unequal prior probabilities only, but some research has also been done on a non-constant assignment of priors. In the case of the SST and SDA, the priors may change between collections or frames due to changing atmospheric conditions. Decisions about how often the priors need to be updated, or the optimal feedback for the priors are not covered in this research. In the next section, the theory for building the optical model, the ECUP algorithm, and assigning the prior probabilities is discussed.

III. THEORY

In order to implement an ECUP detection algorithm, there are three important factors: how the algorithm reduces to a calculable statistic, as well as the performance of the algorithm, and realistic and representative values for the prior probabilities π_k. This section covers the theory developed for these three questions.

A. System Model

To perform the MHT proposed in this paper, an optical model is needed. This model is described in more detail in [1]. The PSF for an optical system is known to be well represented by a Fourier Transform of the pupil function $P(m,n)$.

$$h(x,y) = |\mathcal{F}\{P(m,n)\}|^2 \tag{4}$$

m and n are coordinates in the pupil plane and x and y are pixel coordinates in the focal plane. $\mathcal{F}\{\cdot\}$ is a two-dimensional Fourier transform. The optical model combines several important effects that shape the PSF. The pupil function contains information on telescope parameters as well as Zernike polynomials [31] representing aberrations in the optics. In addition, the effect of a long exposure atmosphere can be modeled by convolving the Fourier transform of the optical PSF with the long exposure Optical Transfer Function (OTF) [10].

There are other methods for creating PSF models [15, 32], but the focus of this paper was not to optimize the PSF. There are also research efforts into reconstructing undersampled PSFs [33, 34]. These methods could potentially reconstruct the SST PSF and remove the need for a MHT, but would require additional processing that may not feasible in the required processing time line. These methods are not used or further investigated in this paper.

The resulting PSF in equation (4) is a representation of the received image before being sampled. Since the pixels are not Nyquist sampled, the aliasing can be added to the equation with the following blurring function, assuming 100 percent fill factor within the array.

$$\begin{aligned} h_k(x,y) = \sum_{x_1=1}^{N_x}\sum_{y_1=1}^{N_y} h(x_1,y_1) \ \times \ldots \\ \operatorname{rect}\left(\frac{\beta x - x_1}{\beta}\right)\operatorname{rect}\left(\frac{\beta y - y_1}{\beta}\right). \end{aligned} \tag{5}$$

x_1 and y_1 are temporary convolution variables, and N_x and N_y are the total number of pixels in the x and y direction respectively. $h_d(x,y)$ represents the convolved and downsampling effects on the PSF of sampling at a frequency greater than Nyquist. β is the undersampling factor. The aliased PSFs can be modeled by changing the location of the object on the highly sampled PSF model, and then downsampled with equation (5). Next, a model for the received data $I(x,y)$ is needed.

$$I(x,y) = \begin{cases} \gamma h_k(x,y) + B & H_k, k \neq 0 \\ B & H_0 \end{cases} \tag{6}$$

γ is the modeled space object intensity. $h_k(x,y)$ is the PSF described in equation (4), and B is the background photo count. A noise model is also needed to represent the conditional Probability Density Function (PDF) present in the Bayes Risk test developed in section III B. For several reasons the noise is assumed to be Gaussian. The multiple sources of noise tend to give an overall Gaussian distribution to the noise present in the system. Another reason is that it has been shown that for a sufficiently high background, as there is in this situation, the both Gaussian and Poisson assumptions lead to a similar algorithm [17, 20]. Additionally, the Gaussian assumption leads to an algorithm where the sufficient statistic is not computationally complex. Alternative noise assumptions are investigated further in [22]. Assuming a Gaussian received noise distribution and that all pixels are independent, the joint probability of the received data $\mathbf{D}$ given H_k can be described with the following:

$$\begin{aligned} p(\mathbf{D}|H_k) = \left(2\pi\sigma^2\right)^{-\frac{N_x N_y}{2}} \times \ldots \\ \exp\left(-\sum_{x=1}^{N_x}\sum_{y=1}^{N_y}\frac{(D(x,y)-I(x,y))^2}{2\sigma^2}\right). \end{aligned} \tag{7}$$

N_x and N_y are the number of pixels in the x and y direction. σ is the measured standard deviation of the received data $D(x,y)$.

B. Deriving Detection Algorithm

The next step is to reduce the Bayes risk from equation (2) with the assumed noise distribution, costs, and priors. Implementing an equal-cost assumption, the Bayes risk test can be reduced to the following relation:

$$\frac{\pi_k p(\mathbf{D}|H_k)}{\pi_0 p(\mathbf{D}|H_0)} \underset{H_0}{\overset{H_k}{\gtrless}} 1 \tag{8}$$

$p(\mathbf{D}|H_k)$ is the conditional PDF of the data, given that hypothesis k is true. In equation (8), the method for determining the hypothesis selected is clear. If the k^{th} hypothesis test is greater than one, it is assumed to have occurred, and the largest of those ratios gives the hypothesis that most likely occurred. A different selection of costs results in a different hypothesis test, but these are not investigated in this paper.

Next, to further reduce the hypothesis test, equation (8), the model for the received data, equation (6), and noise model, equation (7), are combined to give the following equation:

$$\exp\left(\frac{\sum\limits_{x=1}^{N_x}\sum\limits_{y=1}^{N_y}\frac{[D(x,y)-\gamma h(x,y)-B]^2}{2\sigma^2}}{\sum\limits_{x=1}^{N_x}\sum\limits_{y=1}^{N_y}\frac{(D-B)^2}{2\sigma^2}}\right) \underset{H_0}{\overset{H_k}{\gtrless}} \frac{\pi_0}{\pi_k}. \tag{9}$$

Reducing and arranging the left side of the equation to give a correlation between the data and the PSF yields:

$$\begin{aligned} \sum_{x=1}^{N_x}\sum_{y=1}^{N_y}\frac{(D(x,y)-B)}{\sigma}h_k(x,y) \underset{H_0}{\overset{H_k}{\gtrless}} \\ \ln\left(\frac{\pi_0}{\pi_k}\right)\frac{\sigma}{\gamma} + \frac{\gamma\sum\limits_{x=1}^{N_x}\sum\limits_{y=1}^{N_y} h^2(x,y)}{2\sigma}. \end{aligned} \tag{10}$$

Equation (10) shows that that for a equal-prior assumption the natural log of equal priors would be zero. The term would be removed, and the algorithm reduces to the ECEP test proposed in [21]. In an ECUP test this term becomes a weighting term, W.

Grouping the algorithm into a SNR statistic based on the data, and the remaining terms consisting of the prior probabilities and threshold from previous algorithms, the following definitions are made:

$$\text{SNR}_k = \sum_{x=1}^{N_x}\sum_{y=1}^{N_y}\frac{(D(x,y)-B)}{\sigma}h_k(x,y) \tag{11}$$

$$W_k = \frac{\sigma \ln\left(\frac{\pi_0}{\pi_k}\right)}{\gamma} + \frac{\gamma\sum\limits_{x=1}^{N_x}\sum\limits_{y=1}^{N_y} h^2(x,y)}{2\sigma} \tag{12}$$

Exploring each of these terms provides insight into how the algorithm operates. SNR_k is the correlation term between the data $D(x, y)$ and the k^{th} hypothesis PSF. The value of this term determines how much the data resembles the PSF model.

W_k, is effectively a weighting term that modifies the SNR value based on the likelihood of the hypothesis occurring. A weighting term is needed for each hypothesis k, and it can be precomputed for each set of priors and PSFs used. This does not add significant processing time compared to an ECEP test. The second term in the weighting factor is what is traditionally defined as Γ. Γ is traditionally the threshold value that sets the false alarm rate for the hypothesis test. This has been set at 6 for the currently implemented SST BHT, but is modified to 6.2212 to keep a constant false alarm rate in the ECEP MHT presented in [21]. More discussion of setting the desired P_f rates is covered in section III E

Both SNR and W_k have a dependence on k, and are moved to the left side of the equation. Selecting the hypothesis that gives the larges value, indicates which hypothesis is most likely to have occurred. This hypothesis is then compared against the null hypothesis to make a final detection decision.

$$\max_k \left[\mathrm{SNR}_k - W_k\right] \underset{H_0}{\overset{H_k}{\gtrless}} 0 + \tau \tag{13}$$

The algorithm is theoretically compared against zero, but a threshold adjustment τ can be added to achieve different P_f values. Selecting a τ value allows for the algorithm to operate at the desired false alarm rate. Comparing against the proposed ECEP test from [21], the similarities can be quickly observed.

$$\max_k \left[\mathrm{SNR}\right] \underset{H_0}{\overset{H_k}{\gtrless}} \Gamma \tag{14}$$

One noticeable benefit is that the equal cost portion of the algorithm still preserves the ability to select a hypothesis k. In [1] improved detection performance was observed, but the algorithm could only make a binary decision between a space object being present or not. The sub-pixel position information available from the ECEP and ECUP algorithms is shown to be useful in increasing tracking accuracy [35]. Another difference is the additional calculation required for the weighting terms. As mentioned previously, W_k does not depend on the full frame data, and can be computed once per frame to get accurate background standard deviation and updated priors if desired.

As shown, the derived ECUP algorithm is able to be reduced to a sufficient statistic and is not too computationally complex. These are all positive indicators for a successful algorithm. Next, the three methods for determining realistic and accurate prior probabilities are investigated.

C. Decision Space Analysis

A key element to creating an algorithm that takes into account an unequal prior probability scheme is determining the prior probabilities for each sub-pixel hypothesis. Without a method of accurately determining these values, the actual benefit of an ECUP test may not be realized. This paper investigates three potential methods for segmenting the pixel into a decision space. These methods are: a distance-based metric, a correlation metric, and an empirical method. Each method will be described and analyzed.

A critical assumption common with all of these methods is that a space object is equally likely at any position within a pixel. This position, (α, ω), is the physical distance in μm within a 2x2 binned pixel. This assumption implies a uniform probability across the entire pixel. To segment the decision space, a sub-pixel map is created. In the map, each position tested has the same probability of occurrence. To ensure a fine enough coverage of the entire pixel, sub-pixel positions are tested every 1μm in both α and ω. This results in 31 positions in each dimension and 961 positions total.

In this paper, $M = 10$ hypotheses are considered. These hypotheses are PSFs generated through the optical model where a space object is assigned to be in a defined location within a pixel. As previously mentioned, the hypotheses positions are defined by α and ω, the position within a 30x30μm pixel, with the origin being the center of the pixel. The locations within a pixel are the corners where $\alpha = \pm 15$ and $\omega = \pm 15$, sides where $\alpha = 0$ and $\omega = \pm 15$, top and bottom where $\alpha = \pm 15$ and $\omega = 0$, and the center of each pixel.

There are multiple reasons for using these positions. First, they give a fairly even representation of the potential PSFs based on the coverage of the entire pixel. Additionally, they can reduce computational complexity and reduce the number of tests due to sharing the corners and sides between adjacent pixels. Instead of testing all nine alternate hypotheses, only five are needed for each pixel. This scheme was first proposed in [21], an alternate layout of hypothesis positions with $M = 6$ is proposed in [1], but is not investigated in this paper.

The first method considered is the correlation metric. Both the ECEP and ECUP algorithms are based on a matched filter, or correlation test. By determining which hypothesis correlates most closely with each sub-pixel position tested, an assignment matrix can be formed by noting the most closely correlated hypothesis at each sub-pixel position α, ω. This is done with the following equation:

$$\mathcal{H}_c(\alpha, \omega) = \underset{k}{\operatorname{argmax}} \left[\sum_{x=1}^{N_x} \sum_{y=1}^{N_y} \frac{T_{\alpha,\omega}(x, y) h_k(x, y)}{\sigma_k}\right] \tag{15}$$

σ_k is a normalization term based on the k^{th} hypothesis,

$\sigma_k = \sqrt{\sum_{x=1}^{N_x}\sum_{y=1}^{N_y} h_k^2(x,y)}$. $\mathcal{H}_c(\alpha,\omega)$ is an entry in a matrix $\boldsymbol{\mathcal{H}}_c$. Each coordinate represents a sub-pixel position and contains the closest hypothesis match. $T_{\alpha,\omega}(x,y)$ is a 16x16 pixel modeled PSF based on a space object at the sub-pixel location (α,ω). An important note is that the PSFs for $T_{\alpha,\omega}(x,y)$ and $h_k(x,y)$ are generated by performing the appropriate shift on the highly sampled PSF and downsampling as described in equation (5).

The second method for assigning a sub-pixel position to a hypothesis being considered is a distance-based metric. There are several methods for measuring the distance, or size of a vector. In this research a 2-norm is used to find the "closest point" between the sub-pixel position being tested and the locations of the hypotheses.

$$\mathcal{H}_d(\alpha,\omega) = \underset{k}{\operatorname{argmin}} \left(||\vec{V}_k|| \right) \tag{16}$$

$\vec{V}_k$ is a vector between each hypothesis k located at (α_k,ω_k), and the sub-pixel position, (α,ω), being tested. $\mathcal{H}_d(\alpha,\omega)$ is the hypothesis assignment matrix for the distance-based metric. At each point, nine vectors are created and the smallest 2-norm is selected as the hypothesis that best represents the sub-pixel position.

Figure 2 shows the decision space analysis for a single CCD pixel. The plots demonstrate the physical layout of the decision space and the boundaries between each hypothesis. Each sub-pixel position is assigned a corresponding hypothesis, and is grouped into a section with similarly assigned hypotheses.

Looking at the distribution of hypothesis assignments in Figure 2, there are similarities between the correlation and distance based metrics. Both segment the decision space into squares and rectangles based on the location of the hypothesis. The correlation metric has sub-pixel positions between H_5 and H_8 as well as H_4 and H_7 that do not directly create perfect square or rectangle boundaries. These may be due to optical effects not included in the distance metric including aberrations and atmospheric effects.

The final method being considered is an empirical method. This method depends on implementing the ECEP algorithm, and noting the selected hypothesis. One drawback is that it only analyzes objects that it can detect. The inherent assumption is that non-detectable objects will have the same spatial distribution as detectable objects. Using the ECEP algorithm, the following equation can be used to assign sub-pixel positions [21]:

$$\text{SNR}_k = \sum_{x=1}^{N_x}\sum_{y=1}^{N_y} \frac{(D_{x_o,y_o}(x,y) - B)}{\sigma}\frac{h_k(x,y)}{\sigma_k}. \tag{17}$$

$D_{x_o,y_o}(x,y)$ is a data window that is N_x by N_y pixels centered at x_o,y_o.

$$\mathcal{H}_e(x_o,y_o) = \underset{k}{\operatorname{argmax}} \left[\text{SNR}_k\right] \tag{18}$$

These methods all have a hypothesis assignment matrix, $\boldsymbol{\mathcal{H}}$, that gives each sub-pixel position a hypothesis that it most closely resembles. The prior probability values calculated from all three methods are included in section V. One distinction between the methods is that $\boldsymbol{\mathcal{H}}_c$ and $\boldsymbol{\mathcal{H}}_d$ represent a single CCD pixel, while $\boldsymbol{\mathcal{H}}_e$ represents an entire frame of SST data. Therefore, $\boldsymbol{\mathcal{H}}_e$ does not provide insight into how the decision space inside the pixel is physically distributed, only the prior probability of each hypothesis occurring.

D. Investigating Null Hypothesis Probability

In addition to investigating the probability of the alternate hypotheses, $\pi_1 - \pi_M$ the value for the null hypothesis, π_0, needs to be determined. π_0 describes the probability that no RSO is present in the pixel being tested. It is a difficult research problem to determine the likelihood of any space object being present in a specific portion of the sky captured.

All methods described in the previous section divide 100 percent of the decision space between the M hypothesis. This forces the sum of π_1 to π_M to be one. This does not account for the fact that the total probability of all the hypotheses must sum to one, including π_0. To accomplish this, the calculated π_k are adjusted with the following equation:

$$\pi_k' = (1-\pi_0)\pi_k. \tag{19}$$

If there is no concrete method of selecting a value for π_0 there are three potential solutions. One would be to use the same assignment as ECEP, $\pi_0 = 0.10$ since it is the method being compared against. Another option is to investigate the actual value of π_0, but as mentioned earlier this may not be possible. Alternatively, this paper demonstrates that the effect of changing the null hypothesis prior probability does not alter detection performance. To confirm this theory, a constant C is introduced. C acts multiplicatively with π_0, to adjust the null hypothesis value.

$$\begin{aligned} \pi_0' &= C\pi_0 \\ \pi_k' &= (1-C\pi_0)\pi_k \end{aligned} \tag{20}$$

Proposing different values for π_0 can be accomplished by choosing two distinct constants, C_1 and C_2. Computing the difference in weighting, ΔW_k, gives insight into the impact of changing π_0.

$$\Delta W_k = W_k(C_2) - W_k(C_1) \tag{21}$$

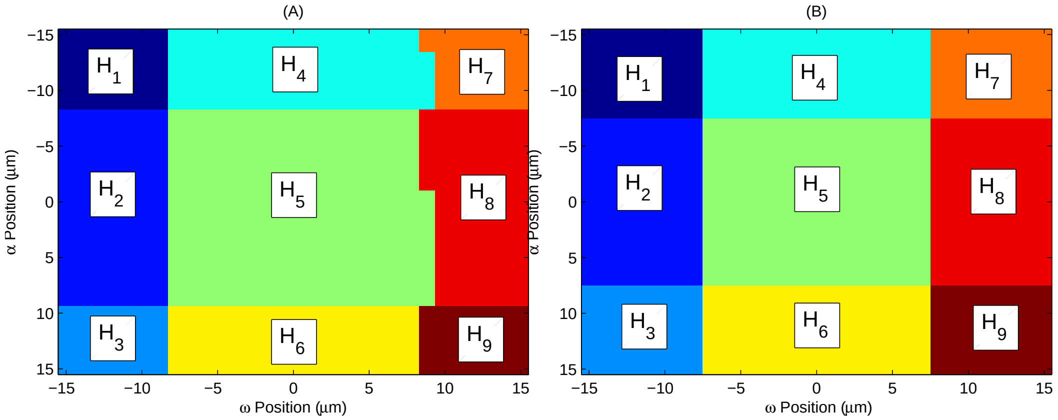

FIG. 2: Decision space analysis for a single SST CCD pixel. The hypothesis assignment matrix for (A) the correlation metric, $\boldsymbol{\mathcal{H}}_c$, and (B) distance metric, $\boldsymbol{\mathcal{H}}_d$. Each color shade corresponds to a similar hypothesis. Sub-pixel positions are tested every 1μm

$W_k(C)$ is the weighting term from equation (12) substituted with updated priors from equation (20). Combining and reducing with constants C_1 and C_2 gives an expression for the change in the k^{th} weighting term due to a change in the null hypothesis prior probability.

$$\Delta W_k = \frac{\sigma}{\gamma} \ln\left(\frac{C_2\pi_0}{(1-C_2\pi_0)\pi_k}\right) - \frac{\sigma}{\gamma} \ln\left(\frac{C_1\pi_0}{(1-C_1\pi_0)\pi_k}\right)$$

$$\Delta W_k = \frac{\sigma}{\gamma} \ln\left(\frac{C_2(1-C_1\pi_0)}{C_1(1-C_2\pi_0)}\right) \qquad (22)$$

Looking at equation (22), ΔW_k is only a function of the constants and the original π_0. This signifies that ΔW_k is independent of k, and it can be moved and grouped into the threshold τ. The constant adjustment to the threshold will change the false alarm, which can be adjusted to match the desired P_f rate. From this analysis it is shown that the assignment for the value of π_0 does not change the detection performance of the algorithm.

E. Setting False Alarm Probability

It is important to ensure that both the ECEP and ECUP algorithms have the same probability of false alarm, P_f. The weighting term, W_k, is effectively changing the threshold and therefore the false alarm probability. Since the weighting term can be different for each hypothesis, the false alarm probability for the entire test needs to account for all hypotheses.

To be able to calculate P_f, the following two assumptions are made. The first is that SNR statistics calculated with equation (11) are Gaussian, which follows logically from the assumption that the received noise is Gaussian. The second assumption is that the probabilities of false alarm for each hypothesis are independent, and can be calculated separately. This assumption is applied to both the ECEP and ECUP algorithms. This assumption may over estimate P_f if there is any dependence between hypotheses, but will do so nearly equally to both algorithms. For the ECEP test, a base threshold of $\gamma = 6$ is used to match previous algorithms and the SST programs threshold. The threshold for ECUP is then adjusted to give both algorithms the same P_f.

To express the method of calculating P_f, the term $\mathcal{N}(\mu, \sigma)$ is defined to represent a Gaussian distribution with mean μ and standard deviation σ. As described previously, the SNR in the ECEP algorithm is normalized to be a zero mean unit variance Gaussian random variable. Since the ECUP algorithm is not normalized by σ_k, SNR_k is no longer zero mean unit variance Gaussian. SNR_k has a mean of W_k and standard deviation of σ_k for each hypothesis.

$$\begin{aligned} &\text{ECEP:} \quad && X \sim \mathcal{N}(0,1) \\ &\text{ECUP:} \quad && X_k \sim \mathcal{N}(W_k, \sigma_k) \end{aligned}$$

Assuming independence between tests, the total false alarm can be calculated by adding the false alarm probability from each alternate hypothesis.

$$P_f = \sum_{k=1}^{M} 1 - p(X \leq \tau) \qquad (23)$$

$p(X \leq \tau)$ is the Cumulative Distribution Function (CDF), and X is a random instance drawn from the Gaussian distribution described by either the ECUP or ECEP test. For the ECEP test, a value of 6 is used for τ. To ensure the tests have the same probability of false alarm, a τ needs to be found that gives equal P_f between the tests.

IV. EXPERIMENT DESCRIPTION

The data analyzed in this paper is from the SST. This data was originally collected as an experiment to test how faint of an object can be detected by different detection algorithms. The SST is programmed to track a communication satellite, ANIK-F1, as it enters eclipse. The resulting intensity loss causes the object to go from easily detectable to difficult to detect.

In addition to the satellite in each image there are thousands of other objects, including stars and potentially RSOs. These stars and other space objects give a large quantity of varying intensity objects to test algorithms against. By processing a large portion of an image and totaling the number of detected objects, a metric of performance can be determined for each algorithm. All types of objects are treated similarly in this algorithm, since both stars and RSOs appear as point source objects to the SST.

Each frame of collected data consists of 6144x4096 pixels, where each pixel contains 2x2 binned 15μm square pixels. The data analyzed in this paper was collected on three nights 13-15 March 2012, referred to as night 073-075 respectively from this point. As mentioned in the optical model description, each image is a long exposure collection.

Within each image there are areas where CCD arrays are aligned, and other areas of imperfection. To remove these effects, a subset of each frame is analyzed. An area consisting of 1024x1024 pixels is selected. This area is consistent through each frame as the data is analyzed. Testing on each pixel is done by including a 16x16 window around the pixel being tested. Including the window gives enough samples to calculate accurate background statistics and contains enough pixels to capture both the PSF model and any space objects. Next, the results for the calculated prior probabilities and the number of detected space objects are presented and analyzed.

V. RESULTS

The first results to discuss, are the calculated values for the prior probabilities π_k. To calculate these probabilities, the total number of each hypothesis present in the hypothesis assignment matrix $\boldsymbol{\mathcal{H}}$ is divide by the total number of sub-pixel positions tested. It is helpful to define the mathematical notation of an Iverson Bracket [36], where $[\cdot]$ gives a value of 1 is true or zero if false the following equation gives the value for the prior probabilities:

$$\pi_k = \sum_{\alpha=1}^{N_\alpha} \sum_{\omega=1}^{N_\omega} \frac{[\mathcal{H}(\alpha,\omega) = H_k]}{N_\alpha N_\omega}. \tag{24}$$

N_α and N_ω are the size of the window being investigated in α and ω. Equation (24) is applied to each hypothesis assignment matrix. The three methods calculating the prior probabilities are shown in Figure 3.

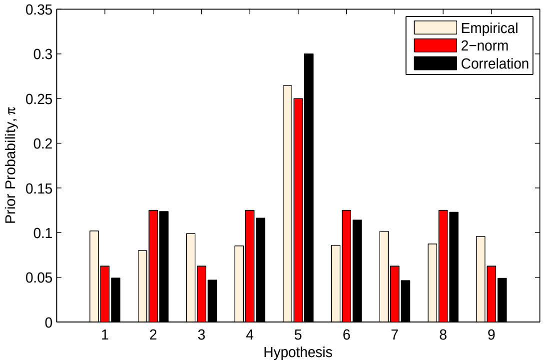

FIG. 3: Comparison of three proposed methods of assigning sub-pixel positions.

Figure 3 shows the prior probabilities for the three methods of segmenting the decision space. The first thing to note is that all three methods give similar prior probability values, with a maximum difference of approximately 10 percent. The general agreement between the priors gives a good indication that the methods accurately represent the true probabilities. The hypothesis at the center of the pixel, H_5, has the largest probability of occurring in all methods. The prior value ranges between 25 to 30 percent. Using a BHT, only one hypothesis is considered and it is that the object is located directly in the center of a pixel. This analysis shows that using a BHT would only match well with 25 to 30 percent of potential objects decreasing the ability to detect space objects.

The methods vary slightly in how they assign probability between the sides and corners. Distance and correlation metrics give higher probability to the sides, while the empirical method favors the corners. The empirical priors for the sides and corners are closer, and the other methods have a larger separation between them. The differences can be due to things not accounted for in the model that occur in measured data such as non-uniform response across the CCD detector areas within pixel. In the empirical method, there is noise present in the data which is not present with the other methods.

Considering the three methods and their resulting priors, this paper uses the empirical method of determining π_k values. This is done due to the fact that it is the closest match to how the ECUP detection algorithm actually operates. Additionally, it includes noise and other details that are not present in the other methods. The distance and correlation metrics also provide confidence that the empirical method is an accurate way to define prior probability since they generally agree. Table II summarizes important details about the locations, prior probabilities with the empirical metric, and the resulting weighting values.

As Table II shows, probability is lower in the cor-

TABLE II: The sub-pixel locations of the M hypotheses (μm) along with the calculated priors π_k and weighting values W_k based on the empirical method.

	$\mathbf{H_1}$	$\mathbf{H_2}$	$\mathbf{H_3}$	$\mathbf{H_4}$	$\mathbf{H_5}$	$\mathbf{H_6}$	$\mathbf{H_7}$	$\mathbf{H_8}$	$\mathbf{H_9}$
α, ω	-15,-15	-15,0	-15,15	0,-15	0,0	0,15	15,-15	15,0	15,15
π_k	0.10	0.08	0.10	0.09	0.26	0.09	0.10	0.08	0.10
W_k	1.78	2.57	1.78	2.56	3.75	2.56	1.78	2.56	1.78

ners and sides with the additional probability shifted to H_5, or the center pixel hypothesis. This implies that it is more likely for captured data to closely match the PSF generated assuming the object is in the center of the pixel. Based on the empirical method, H_5 hypothesis has approximately a 26 percent chance of occurring. The weighting values, W_k, from equation (12) which are calculated based on π_k also provide interesting results. All of the weighting values are positive, and W_k is subtracted from the computed SNR. The newly computed SNR compared against the threshold will be lower than the ECEP test. This is counteracted by the new threshold τ computed to ensure equal P_f rates. Although the weighting term is a linear effect on the SNR, calculating τ is not linear. Considering these two competing effects, it is difficult to analyze how this will increase or decrease the number of RSOs detected. This is why collected telescope data detection performance is analyzed.

After assigning priors, the ECUP algorithm can be implemented on collected data. To accomplish this, the data described in section IV is analyzed. This data contains many different intensity level objects, including many much greater than the current threshold. These objects will be easily detectable with both the ECEP and ECUP algorithm. The difference in detection is the RSOs that are close to the detection threshold. Objects much brighter than this will easily be detected with both and space objects much dimmer than the threshold will not be detected by either algorithm.

There are a couple of potential methods for reporting the change in detection performance. Using a probability of detection, P_d, at a specified false alarm rate P_f is a commonly used metric. Another method is reporting P_d across a large range of potential P_f values, also known as a Receiver Operating Characteristic (ROC) curve typically provides insight. In this paper, the number of additional detected objects at a specified false alarm is reported. The difference in the number of detected objects between ECEP and ECUP is defined as Δ_o:

$$\Delta_o = \text{ECUP} - \text{ECEP}. \tag{25}$$

The total number of detected objects includes all alternate hypotheses where an object is considered present, H_1 through H_9. Using the calculated P_f value of 8.5e-09, and $\tau = 6$ for ECEP and $\tau = 0.98$ for ECUP, the SST data is analyzed. Figure 4 demonstrates the difference in the number of detected object between ECUP and ECEP.

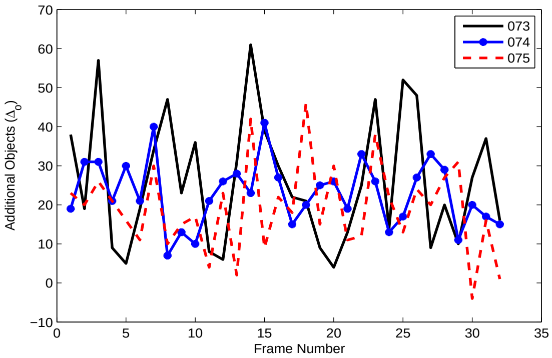

FIG. 4: Difference in number of detected objects, Δ_O, over 32 sample frames from data collects on night 073-075.

Δ_o ranges from 61 additional objects to four less objects on the days and frames processed. Across all three nights processed there were, on average, more objects detected with ECUP. For each frame, the total number of detected objects changes as objects enter and exit the frame, noise spikes occur, and space objects change intensity. Δ_o stays fairly consistent through these changes. There is an obvious increase in detected objects present in the sample data analyzed, but it is important to ensure that it is not a random occurrence. One method is to perform a significance analysis on the mean. Looking at a paired T statistic test can indicate if there truly is a different in means and which is greater [37]. Night 073 has a paired T test statistic value of 9.07. This signifies it is highly likely that ECUP is detecting more objects on average than ECEP. Large T statistic values also occurred on nights 074 and 075, 15.62 and 9.49 respectively.

Additional information can be gleaned from investigating the distribution of Δ_o data. Figure 5 shows a histogram for Δ_o across all three nights of the SST data processed.

The distribution of the additional number of detected objects appears Gaussian. Across all of the processed data, Δ_o has a mean of 22.73 and a standard deviation of 12.65. Table III shows the average number of additional detected objects and standard deviation of the ECUP algorithm for individual nights.

One noticeable result from Table III is that the largest Δ_o occurred on night 073. This was the night used to generate the priors with the empirical method. This signifies two interesting details. The first is that the empirical priors do not necessarily need to be recomputed frequently. The empirical priors are able to achieve an improvement for three consecutive nights without adjustment. The values do decrease slightly between nights. Several factors including atmospheric conditions may cause the priors to change slightly between collections. There may be

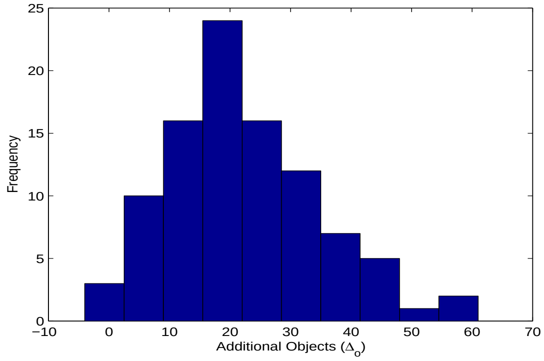

FIG. 5: Combined histogram for Δ_o. All nights analyzed 073-075 are included.

TABLE III: Average number of additional objects detected by ECUP, $\bar{\Delta}_o$, and standard deviation, σ_{Δ_o}, for three nights 13-15 March 2012.

	Night 073	**Night 074**	**Night 075**
$\bar{\Delta}_o$	26.13	22.97	19.10
σ_{Δ_o}	16.30	8.32	11.38

an optimal update rate for priors that takes these factors into account, but this is not further investigated in this paper.

The sub-set of frames analyzed for this paper are not the full image frames. Increasing the number of pixels being tested would also increase Δ_o. A total of 24 of the 1024x1024 frames are in the full frame data. Applying the averages determined in the small frame would give approximately 458-627 additional objects on average.

An important factor in determining usefulness for a new algorithm is possibility of adding computational cost. Using ECUP Δ_o does not give a large gain in the percent of increased objects, but it also does not add significant computational cost. The empirical method for generating priors only needs to be updated periodically and is not a significant consideration. The ECUP algorithm adds an addition or subtraction to each hypothesis being tested. These M additions are not significant compared to the computation time of the correlation operation performed in both algorithms.

VI. CONCLUSIONS

This paper demonstrates that for certain applications it may be beneficial to use an ECUP MHT algorithm. It was shown that with high statistical confidence the ECUP algorithm detects on average more objects than an ECEP algorithm performed on the SST data. For the small sub-set of the frames analyzed 19.10-26.13 additional objects were detected, which translates to 458-627 additional objects on average for full frame data. These objects are most likely threshold objects that are difficult for currently proposed detection algorithms to detect. Finding these threshold objects will provide additional information for tracking and characterization, in turn increasing the SDA picture.

In addition, a method of using empirical observations of representative data is developed to form a model for a priori probabilities. Distance and correlation metrics were also considered and resulted in similar distribution of prior probabilities.

The ECUP algorithm assumed Gaussian received noise in this paper. A possible future research are could investigate removing the Gaussian assumption which may result in the detection of additional space objects. In other possible future research, additional methods can be combined to potentially improve detection performance even further. For example, using an unequal-cost and an unequal-prior probability scheme may improve over a unequal-cost equal-prior test.

In the ECEP MHTs, the threshold is considered constant for each hypothesis. As a result, the modeled intensity is effectively different for each hypothesis, as dependent on the distribution of the PSF. This assumption is changed in this paper for the ECUP algorithm. This assumption can be removed in a future ECEP test, and may provide interesting research opportunities and advancements.

Another consideration is how including unequal-priors may affect the ability to translate the detected objects into accurate tracking and orbit determination. The ECUP algorithm takes into account the probability of the alternate hypotheses, each of which correspond to a sub-pixel position. The sub-pixel information gathered from performing a ECUP test may lead to improved sub-pixel position and in turn more accurate tracking of detected RSOs.

This material is based upon work sponsored by DARPA. The views expressed are those of the authors and do not reflect the official policy or position of the Department of Defense or the U.S. Government.

[1] T. Hardy, S. Cain, J. Jeon, and T. Blake, "Improving space domain awareness through unequal-cost multiple hypothesis testing in the space surveillance telescope,"

Appl. Opt., vol. 54, pp. 5481–5494, Jun 2015.

[2] Department of Defense Directive 3100.10, “Space policy,” 2012.

[3] United States Government, “NATIONAL SPACE POLICY of the UNITED STATES of AMERICA,” 2010.

[4] J. Finch, “Sustainability and the National Security Space Strategy: an Approach to the Congested Environment,” 2012. Office of the Under Secretary of Defense for Policy.

[5] R. Willstrop, “The mersenne–schmidt: a three-mirror survey telescope,” *Monthly Notices of the Royal Astronomical Society*, vol. 210, no. 3, pp. 597–609, 1984.

[6] Defense Advanced Research Projects Agency (DARPA), “Space Surveillance Telescope (SST) - Our Work.” `http://www.darpa.mil/Our_Work/TTO/Programs/Space_Surveillance_Telescope_(SST).aspx`, 2014. [Online; accessed 2-June-2014].

[7] United States Government, “Public Law 109-155, NASA Authorization Act 2005,” 2005. 109th United States Congress.

[8] Committee to Review Near-Earth Object Surveys and Hazard Mitigation Strategies Space Studies Board; National Research Council, *Defending Planet Earth:Near-Earth Object Surveys and Hazard Mitigation Strategies*. The National Academies Press, 2010.

[9] P. Martin, “NASAs Efforts to Identify Near-Earth Objects and Mitigate Hazards,” tech. rep., NASA Inspector General, 2014.

[10] J. Goodman, *Statistical Optics*. New York: John Wiley & Sons, Inc, 2000.

[11] J. Scotti, “Near-earth object surveying in the late 20th century,” in *Completing the Inventory of the Solar System*, vol. 107, pp. 107–113, 1996.

[12] H. Viggh, G. Stokes, F. Shelly, M. Blythe, and J. Stuart, “Applying Electro-Optical Space Surveillance Technology to Asteroid Search and Detection: The Linear Program Results,” in *Proceedings of the 1998 Space Control Conference*, 1998.

[13] E. Bertin and S. Arnouts, “Sextractor: Software for source extraction,” *Astronomy and Astrophysics Supplement Series*, vol. 117, no. 2, pp. 393–404, 1996.

[14] E. Bertin and M. Dennefeld, “Galaxy evolution at low redshift?–i. optical counts,” *Arxiv preprint astro-ph/9602110*, 1996.

[15] E. Bertin, “Automated morphometry with sextractor and psfex,” in *Astronomical Data Analysis Software and Systems XX*, vol. 442, p. 435, 2011.

[16] P. Gural, J. Larsen, and A. Gleason, “Matched filter processing for asteroid detection,” *The Astronomical Journal*, vol. 130, no. 4, p. 1951, 2005.

[17] S. Pohlig, “An Algorithm for Detection of Moving Optical Targets,” *IEEE Transactions on Aerospace and Electronic Systems*, vol. AES-25, no. 1, pp. 56–63, 1989.

[18] A. O’Dell, “Detecting Near-Earth Objects Using Cross-Correlation with a Point Spread Function..” Air Force Institute of Technology AFIT/GE/ENG/09-30, 2009.

[19] G. Healey and R. Kondepudy, “Radiometric CCD Camera Calibration and Noise Estimation,” *Pattern Analysis and Machine Intelligence, IEEE Transactions on*, vol. 16, pp. 267–276, Mar 1994.

[20] C. Peterson, “Near Earth Object Detection using a Poisson Statistical Model for Detection on Images Modeled from the Panoramic Survey Telescope & Rapid Response System..” Air Force Institute of Technology AFIT/GE/ENG/12-33, 2012.

[21] J. Zingarelli, E. Pearce, R. Lambour, T. Blake, C. Peterson, and S. Cain, “Improving the Space Surveillance Telescope’s Performance Using Multi-Hypothesis Testing,” *The Astronomical Journal*, vol. 147, no. 5, p. 111, 2014.

[22] T. J. Hardy and S. C. Cain, “Characterizing point spread function (psf) fluctuations to improve resident space object detection (rso),” in *SPIE Defense+ Security*, pp. 946904–946904, International Society for Optics and Photonics, 2015.

[23] J. Goodman, *Introduction to Fourier Optics*. Englewood, Co: Roberts & Company, 3rd ed., 2005.

[24] H. V. Trees, *Detection, Estimation, and Modulation Theory*. John Wiley and Sons, Inc., 1968.

[25] N. Goodman, P. R. Venkata, M. Neifeld, *et al.*, “Adaptive waveform design and sequential hypothesis testing for target recognition with active sensors,” *Selected Topics in Signal Processing, IEEE Journal of*, vol. 1, no. 1, pp. 105–113, 2007.

[26] M. D. Richard and R. P. Lippmann, “Neural network classifiers estimate bayesian a posteriori probabilities,” *Neural computation*, vol. 3, no. 4, pp. 461–483, 1991.

[27] J. Ediriwickrema and S. Khorram, “Hierarchical maximum-likelihood classification for improved accuracies,” *Geoscience and Remote Sensing, IEEE Transactions on*, vol. 35, no. 4, pp. 810–816, 1997.

[28] R. M. Everson and J. E. Fieldsend, “Multi-class roc analysis from a multi-objective optimisation perspective,” *Pattern Recognition Letters*, vol. 27, no. 8, pp. 918–927, 2006.

[29] F. B. Butar and P. Lahiri, “On measures of uncertainty of empirical bayes small-area estimators,” *Journal of Statistical Planning and Inference*, vol. 112, no. 1, pp. 63–76, 2003.

[30] K. R. Varshney and L. R. Varshney, “Quantization of prior probabilities for hypothesis testing,” *arXiv preprint arXiv:0805.4338*, 2008.

[31] R. Noll, “Zernike Polynomials and Atmospheric Turbulence,” *J. Opt. Soc. Am.*, vol. 66, pp. 207–211, 1976.

[32] S. Paulin-Henriksson, A. Refregier, and A. Amara, “Optimal point spread function modeling for weak lensing: complexity and sparsity,” *Astronomy & Astrophysics*, vol. 500, no. 2, pp. 647–655, 2009.

[33] J. Anderson and I. R. King, “Psfs, photometry, and astrometry for the acs/wfc,” *ACS Instrument Science Report*, vol. 1, 2006.

[34] T. R. Lauer, “Combining undersampled dithered images,” *Publications of the Astronomical Society of the Pacific*, vol. 111, no. 756, pp. 227–237, 1999.

[35] A. Sligar, “Measuring Angular Rate of Celestial Objects using the Space Surveillance Telescope..” Air Force Institute of Technology AFIT-ENG-MS-15-M-019, 2015.

[36] D. E. Knuth, “Two notes on notation,” *American Mathematical Monthly*, pp. 403–422, 1992.

[37] J. S. Milton and J. C. Arnold, *Introduction to probability and statistics: principles and applications for engineering and the computing sciences*. McGraw-Hill, Inc., 2002.